Homogenization of Optical Field in Nanocrystal-Embedded Perovskite Composites

Yuchen Hou[1#], Jun Zhang[2#], Xianlin Zheng[2], Yiqing Lu[3], Alexej Pogrebnyakov[1,4], Haodong Wu,[1] Junjin Yoon,[1] Dong Yang,[1,4] Luyao Zheng,[1] Venkatraman Gopalan[1,4], Thomas M. Brown,[5] James A. Piper[2*], Kai Wang[1,4*], Shashank Priya[1,4*]

[1] Department of Materials Science and Engineering, Pennsylvania State University, University Park, PA 16802, USA

[2] Department of Physics and Astronomy, Macquarie University, Sydney, New South Wales 2109, Australia

[3] School of Engineering, Macquarie University, Sydney, New South Wales 2109, Australia

[4] Materials Research Institute, Pennsylvania State University, University Park, PA 16802, USA

[5] CHOSE, Department of Electronic Engineering, Universitàdegli Studi di Roma Tor Vergata, Rome 00133, Italy

Abstract

Photonic upconversion of in-band transparent light into shorter-wavelength light has been proposed as one of the strategies to exceed the Shockley-Queisser (SQ) limit of 33% in single-junction solar cells. There have been many reports showing the effectiveness of incorporating upconversion (UC) materials (e.g., upconversion nanoparticles (UCNPs)) to enhance the power conversion efficiency (PCE) of solar cells, however so far, there is no demonstration of a real device with PCE exceeding the SQ limit. To understand this paradoxical question, here we use a typical UCNP (composition of $NaYb_{0.99}Tm_{0.01}F_4$) with halide perovskite platform to quantify why the UC mechanism fails to provide a noticeable PCE improvement in solar cells. Firstly, results show that the UC-induced photocurrent gain has a maximal value of 96 pA cm^{-2} (in an ideal monolayer dispersion model) which is negligible compared to the photocurrent (ca. 22 mA cm^{-2}) generated by perovskite itself from the visible spectrum. This is due to the low absorption and quantum yield of the UC materials. Secondly, we demonstrate that by incorporating UCNPs and even nanoparticles (NPs) without UC, there is a redistribution of the optical field occurring in the photoactive layer, leading to a homogenization of optical field (HOF). Such a HOF effect can lead to reduced bimolecular recombination and provide photocurrent enhancement (ca. 7%). This HOF mechanism, instead of the conventional UC mechanism, can explain the general photocurrent enhancement in solar cells with incorporation of nanomaterials.

#Equal contribution

*Correspondences: KW: kaiwang@psu.edu; JP: jim.piper@mq.edu.au; SP: sup103@psu.edu

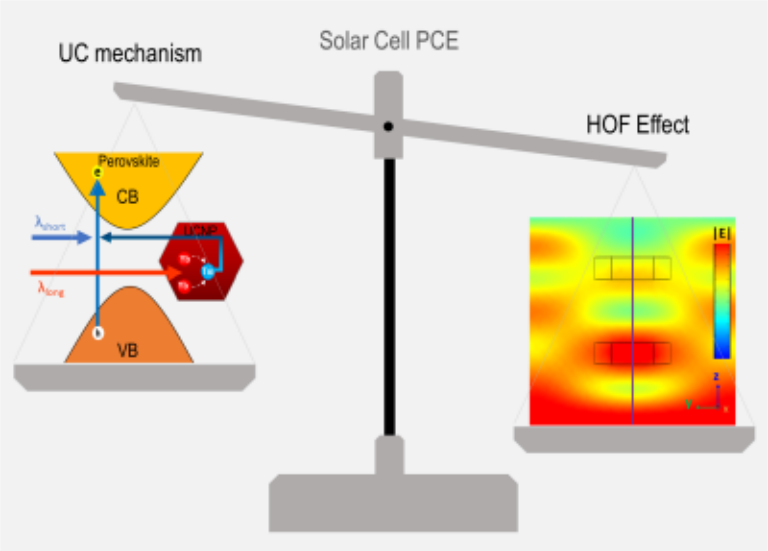

Graphic table of content (TOC)

Introduction

Single-junction solar cells have an upper limit on efficiency of ~33%, set by the Shockley–Queisser (SQ) theory[1], mainly owing to the energy mismatch between the broad wavelength distribution of sunlight and the fixed mono-bandgap of the photoactive material in the cell. 'Thermalization loss' and 'in-band transparency' are the two major loss pathways for power conversion efficiency (PCE), accounting for over 55% loss of the total energy.[2] Many strategies *via* manipulation of hot carrier and multiexciton generation (MEG)[3] or singlet fission[4-5] have been proposed to address 'thermalization loss' pathways. However, the 'in-band transparency loss' has yet to be circumvented to pave the avenue towards PCE exceeding SQ limit. The 'in-band transparency loss' could lead to up to ~18% PCE loss for ideal bandgap solar cells.[1] The long wavelength light (e.g., near infrared (NIR) and infrared (IR) light) having the photon energy smaller than the bandgap of the photoactive material cannot photonically excite the electrons from valance to conduction band but alternatively can be absorbed by molecular vibration to generate unwanted heat (e.g., operating solar cells under AM 1.5 solar radiation can result in temperatures as high as 70 °C at equilibrium[6]). In order to recycle the long wavelength light, one solution is to upconvert transmitted sub-bandgap photons into above-bandgap light that can be further utilized in solar cells.[7] For example, NIR region (800 nm to 2.5 μm) has a total power density of ~ 42 mW cm^{-2} (~ 42% of total solar energy of AM 1.5), thus full utilization of this power density by upconversion (UC) mechanism could theoretically contribute to an addition of photocurrent of 56.5 mA cm^{-2} (assuming an external quantum efficiency (EQE) of 90%). However, whether these strategies are practically achievable remains to be proven[8], where one major obstacle is the low upconversion efficiency of currently existing UC materials.

Upconversion nanoparticle (UCNP) and triplet–triplet annihilation (TTA) chromophore both can display the upconversion behavior from near infrared (NIR) to visible region but with a relatively low quantum efficiency and a nonlinear dependence on light intensity. For example, $NaGdF_4$: 20% Yb^{3+}, 2% Er^{3+} (UCNP)[9] displays an UC quantum efficiency of ca. 1% under 980 nm light with a high excitation intensity of 10^6 mW cm^{-2}, but has only ca. 0.1% UC quantum efficiency under excitation of 10^5 mW cm^{-2}. State-of-the-art $NaYF_4$: 18% Yb^{3+}, 2% Er^{3+} UCNP[10] could reach highest UC quantum efficiency to 10% under an excitation intensity of 5×10^5 mW cm^{-2} but decrease to ~1 % when excitation intensity decreases to 10^4 mW cm^{-2}. Typical TTA UC materials such as $PtAg_{24}(SR)_{18}$/Perylene[11] (sensitizer/annihilator couple) system display an UC

quantum efficiency of 1.1% under 785 nm light excitation of 1.5×10^4 mW cm^{-2}, and the state-of-the-art [PbS-CdS/5-CT (T)]/rubrene[12] system can display a quantum efficiency of 8.4 % under 808 nm excitation. However, these UC quantum efficiencies are heavily dependent on excitation light intensity, and could be much lower under solar light condition (e.g., in the order of 1 mW cm^{-2}) due to their nonlinear nature.[13-14] It remains unclear if the UC strategy could be an effective or reliable strategy to address the 'in-band transparency loss' issue in order to improve the solar cell efficiency based on the currently existing UC nanomaterials.

In parallel to UC mechanism, incorporation of the nanomaterials into solar cells may also trigger other effects, which however is less understood in literature. For example, the presence of UC nanomaterials within the solar cell could modulate the optical field distribution throughout the device due to the large difference in optical parameters such as refractive index and extinction coefficient between the UC nanomaterials and the functional layer in a cell. The light energy density ($|\boldsymbol{E}|^2$) is proportional to the number of photons[15], and thus, the light intensity distribution can be modulated through addition of nanomaterials. This will cause a redistribution of photogeneration site within the device and eventually affect carrier drift distance towards corresponding electrodes, as well as the radiative (bimolecular) recombination probability since it is a function proportional to the square of carrier concentration (localized high carrier concentration can lead to significant recombination loss). These fundamental effects are not well understood and the effectiveness or role of UC nanomaterials in a solar cell remains ambiguous. Particularly in perovskite solar cells, with the high light absorption coefficient (e.g., ~10^5 cm^{-1} for $MAPbI_3$)[16] of perovskite layer, there is a stronger light absorption close to the front surface region whereby higher concentration of photocarriers generated, which could hypothetically lead to severe bimolecular recombination losses in this region. Secondly, along the thickness direction the average photocarrier generation center will offset from the geometric center of the film, leading to unbalanced carrier drift length between electrons and holes. This can increase the probability of scattering and losses of charge carriers and thereby compromise the device performance.

In theory, incorporation of UC nanomaterials into a solar cell can provide the opportunity to exceed the SQ limit. There have been many reports on dye-sensitized solar cells (DSSCs)[17-18], organic photovoltaics (OPVs)[19-20] and perovskite solar cells[21-22] utilizing the UC strategy to improve PCE. Most of these results serve as concept description for illustrating the UC mechanism that could increase the efficiency. However, there is lack of in-depth quantitative analysis related

to the magnitude of UC contribution[8]. There could be many secondary effects occurring in conjunction with the UC mechanism upon incorporation of functional UC nanomaterials, which remains less investigated. Here we introduce the Yb, and Tm-based UCNPs ($NaYb_{0.99}Tm_{0.01}F_4$) in perovskites as a tool to quantitively distinguish the contribution of UC effect with other mechanisms such as abovementioned optical field redistribution and electrical transport modulation. We incorporate the $NaYb_{0.99}Tm_{0.01}F_4$ UCNPs into the $MAPbI_3$ perovskite matrix resulting in a composite structure where UCNPs are embedded in $MAPbI_3$. Next, we construct a solar cell using this composite and observe a photocurrent enhancement of ~7%, which we demonstrate in this study that it does not originate from the UC mechanism as evidenced by both quantum efficiency calculation and EQE measurement. Rather we find that the incorporation of UCNPs in perovskite can flatten the distribution of optical field (verified by field simulation) and consequently avoid photocarrier localization, resulting in a uniform distribution of photocarrier gradient throughout the film. This is highly beneficial for minimizing the photocarrier losses during charge drift and localized bimolecular recombination as well. To further confirm this mechanism, we replaced UCNPs with the non-UC nanoparticles (NUC NP, $NaYbF_4$) and other commercial nanoparticles (SiO_2) of similar optical feature, and observed similar photocurrent improvement effect.

Overall, by using these tools we quantify that under typical solar intensity (AM 1.5) the up-limit contribution to a cell from the state-of-the-art UCNP materials such as $NaYF_4$:Yb/Er is as small as an order of ~ 96 pA cm^{-2}, negligible to the photocurrent (~ 22 mA cm^{-2}) generated from perovskite itself. Nonetheless, a secondary mechanism that we name as 'homogenization of optical field (HOF)' triggered by the incorporation of nanoparticles can contribute a higher photocurrent gain (1.5 mA cm^{-2}). Compared to UC mechanism, the photocurrent enhancement from HOF is ca. $10^7\times$ greater (**Scheme 1**). We show that this HOF mechanism can explain the high photocurrent and low carrier loss in many photovoltaic models using nanostructured materials. Furthermore, we anticipate that these NP-modified cells will be more effective for future applications in condition of high photonic intensity such as light-concentrated solar cell and high energy photovoltaic converter for laser-based wireless energy transmission.

Result and Discussion

Lanthanide upconverters have been used in solar cells based on GaAs, a-Si, c-Si, and DSSC with evidence of efficiency enhancement.[23-26] In perovskite solar cell, the utilization of UCNP (e.g., $NaYF_4:Yb^{3+}/Er^{3+}$) embedded between the charge transport layer and electrode to harvest extra NIR light has also been reported.[22] In principle, the upconversion nanomaterials can be applied either as an electrically isolated layer at the outside of the electrode for manufacturing simplicity, or they can be introduced into the device to minimize optical losses.[8] Incorporating UC nanomaterials such as UCNP within the photoactive layer has been widely reported in DSSC, OPV and perovskite solar cell.[18, 27-28] Here we use the $NaYb_{0.99}Tm_{0.01}F_4$ upconversion nanoparticles (UCNPs) with 1% of Tm being doped in the $NaYbF_4$ matrix (**Fig. 1a**) to form a composite of UCNP: perovskite and study the enhancement in photocurrent. The average size of nanoparticles is ca. 140 nm as shown in the TEM (transmission electron microscopy) image in **Fig. 1b**. Instead of using the typical hexagonal-phase Yb/Tm doped $NaYF_4$ (e.g., $NaY_{0.79}Yb_{0.20}Tm_{0.01}F_4$),[29] here we use the heavily doped UCNP with all the Y^{3+} in the lattice replaced by the sensitizer ion Yb^{3+}, which can maximize the absorption of NIR excitation from solar spectrum.[30-31] **Fig. 1c** shows the typical absorption and photoluminescence spectra of $NaYb_{0.99}Tm_{0.01}F_4$, with the absorption centered around 980 nm and three major emission peaks located around 300-400 nm, 400-500 nm, and 750-850 nm. These emission bands match well with the absorption spectrum of typical perovskite materials, which can be utilized to covert the NIR region of solar spectrum to additional current. Details of each emission band and corresponding energy-level diagram is described in **Supplementary Note 1** and **Fig. S1**.

In order to incorporate the UCNPs into the perovskite matrix, here we utilize the volatile solution (VS) system to prepare the perovskite crystal according to our prior reports[32-34], where the mixed volatile solvent of ethanol and acetonitrile is more compatible with the dispersion degree of the UCNPs. As expected, we obtain the composite with well-dispersed UNCPs into the perovskite (as illustrated in **Fig. 1d**). **Fig. 1e** presents the top-view SEM (scanning electron microscopy) image of the composite film. Most UCNPs are embedded in the perovskite film and only a few are exposed on the surface. The incorporation of UCNPs does not significantly affect the crystalline feature of the perovskite matrix, as can be verified by the identical grain size to that of a reference pristine perovskite film (**Fig. S2**). We also measure the XRD (X-ray diffraction) of the composite film (**Fig. 1f**). Consistent to that of pristine perovskite, there is no impurity peaks from precursors and two prominent peaks located at 14.07° and 24.18° correspond to (110) and

(220) planes of tetragonal (space group *I4/mcm*)[35] $MAPbI_3$, respectively. It is noted that the film show strong orientation preference along (110) and (220) planes, which is commonly observed in the perovskite films fabricated using the same volatile solvent method in prior studies[36-39]. The presence of UCNPs did not change the preferential orientation of film on (110) and (220) planes, implying UCNPs did not interfere with crystallization and growth of the film. To understand the distribution of UCNPs within the film, we use SEM EDS (energy-dispersive X-ray spectroscopy, with electron acceleration voltage of 8 kV; penetration depth ca. 2 μm > film thickness of 0.5 μm) to map the distribution of the embedded UCNPs. **Fig. 1g(i)** displays a larger scale SEM image of the composite film where a few UCNPs can be observed at the surface. **Fig. 1g(iii)** and **1g(iv)** show the element mapping of I and Pb from the perovskite, while **Fig. 1g(v)** to **1g(viii)** show the elemental mapping of Yb, Tm, Na and F from UCNP, respectively. Notably, there is a larger amount of UCNPs that have been embedded in the perovskite film. These results indicate the well-formed composite of $NaYb_{0.99}Tm_{0.01}F_4$ UCNPs in $MAPbI_3$ with excellent crystalline feature of the perovskite.

We then use the composite ($MAPbI_3$/0.2 wt% UCNP) as the photoactive layer in a solar cell with n-i-p configuration of FTO/TiO_2/perovskite/Spiro-OMeTAD/Au to investigate the UC generated photocurrent contribution. For comparison study, we also use a pristine $MAPbI_3$ prepared from same volatile solvent methods in the identical device as a reference, which has no UC effect. **Fig. 2a** compares the cross-sectional SEM of both devices. It can be seen from the composite sample, the embedded UCNPs are well dispersed inside of the perovskite film. All the other layers are controlled in an identical condition for both samples. **Fig. 2b** shows the current density-voltage (J-V) curves of solar cells measured under one-sun illumination (AM 1.5). The control device displays a J_{SC} of 22.93 mA cm^{-2}, V_{OC} of 1.061 V, FF of 76.8% and PCE of 18.66%, consistent with typical values using same composition and device structure[32]. In comparison, the device with the $NaYb_{0.99}Tm_{0.01}F_4$:$MAPbI_3$ composite displays an enhanced J_{SC} of 23.76 mA cm^{-2} (increased by 0.83 mA cm^{-2}) and comparable V_{OC} and FF of 1.048 V and 77.1%, respectively. As a result, a higher PCE of 19.20% has been observed in the composite device. This is consistent with typical observations on photocurrent enhancement in UCNP incorporated solar cells in prior reports[28].

In order to understand if the enhanced photocurrent is driven by the UC mechanism, we further measure the EQE spectra for both devices. In principle, the EQE quantifies the yield of

photocarriers upon scanning of monochromatic light. It can be seen in **Fig. 2c** that the composite device exhibits an overall enlarged EQE spanning from 350 to 775 nm (shadow area in **Fig. 2c**). However, beyond 825 nm, both devices exhibit identical curve with no photocurrent generation (**Fig. 2c**). The $NaYb_{0.99}Tm_{0.01}F_4$ UCNP has an absorption in NIR from 900 nm to 1050 nm with peak value at 980 nm. By incorporating the UCNP into the composite device, there is no photocurrent generation in this region, even under a reverse bias of -0.4 V (**Fig. 2d**) that strengthens the electric force for drifting of any generated photocarriers. We did not observe UC contribution to photocurrent in the NIR region from EQE spectrum, which in fact can be ascribed to the ultralow upconversion quantum efficiency (e.g., 0.1%[9]) of the typical UCNP materials, as discussed below.

In order to understand the results in **Fig. 2d**, we quantitively analyze the theoretical maximum photocurrent that can be generated from upconversion of NIR light using the $NaYb_{0.99}Tm_{0.01}F_4$ UCNPs (detailed in **Supplementary Note 2**). The overall UC-generated photocurrent can be determined from equation of:

$$I_{ph} = q \cdot \int_{\lambda_0}^{\lambda_1} \Psi_{ph,\lambda} \cdot Abs_{UCNP}(\lambda) \cdot \phi_{UC}(\lambda, I) \cdot \eta_{ET}(\lambda) \cdot EQE_{PVK}(\lambda) \qquad (1)$$

where q is the elementary charge, $\Psi_{ph,\lambda}$ [m^{-2} s^{-1}] is the photon flux at wavelength of λ in the solar spectrum, Abs_{UCNP} is the absorption of UCNP, ϕ_{UC} is the upconversion efficiency of the UCNP, η_{ET} is the energy transfer efficiency from UCNP to perovskite, and EQE_{PVK} is the external quantum efficiency of perovskite's photovoltaic process. The integrating range of $[\lambda_0, \lambda_1]$ is in the NIR region, and for the specific case of $NaYb_{0.99}Tm_{0.01}F_4$ UCNP this range is from 950 to 1050 nm, where $MAPbI_3$ perovskite cannot absorb. By assuming the ideal case with negligible energy loss in energy transfer and photovoltaic process (e.g., 100% η_{ET} and EQE_{PVK}), the overall UC-generated photocurrent is calculated to be 96 pA cm^{-2} under AM 1.5 standard solar light. This value is negligible (0.5%) compared to the photocurrent generated from visible light in perovskite solar cells (i.e., > 20 mA cm^{-2}), which is mainly because of the ultralow ϕ_{UC} of 0.01% under NIR intensity of solar spectrum (in the order of 1 mW cm^{-2}) of the UCNPs[40] as well as their low effective absorption efficiency (0.16%). Although other UC materials can reach to a ϕ_{UC} as high as 10 %, but this can only be achieved at very high light intensity of ~10^5 mW cm^{-2} far beyond the NIR intensity in solar spectrum.[41-42] This makes it most likely that the UC mechanism is not responsible for generating additional photocurrent in perovskite solar cells.

Although the UC mechanism did not show noticeable contribution to the photocurrent, the overall improvement of PCE is observed in the composite device similar to that in prior reports[21-22, 28]. To verify this enhancement in PCE, we conducted a statistical study on photovoltaic parameters extracted from multiple devices. A total of 20 devices are fabricated for both control and composite cases and **Fig. 2e** shows the statistics for V_{OC}, FF, J_{SC} and PCEs. The composite devices display an average V_{OC} and FF of 1.07 ± 0.01 V and 75.5 ± 1.5%, respectively, comparable to those of 1.05 ± 0.02 V and 73.6 ± 2.2% from the control devices. In comparison, there is a clear improvement of 6% in J_{SC} from 22.90 mA cm^{-2} of control device to 24.13 mA cm^{-2} of composite device, leading to a 10% enhancement in PCE, from 17.75% of control to 19.46% of composite device. To further confirm the positive contribution of UCNPs on photocurrent, we adjust the concentration of UCNPs in the perovskite matrix and fabricate solar cells to convincingly evaluate their effectiveness on PCEs. We use same device configuration and fabricate 20 devices for each concentration condition. **Fig. 3a** shows the statistics of photovoltaic parameters of solar cells with different UCNP concentrations (detailed in **Table S1**). With UCNP concentration from 0 to 0.2 wt% and to 1.0 wt%, there is a gradual increase in average J_{SC} from 22.46 mA cm^{-2} to 23.53 mA cm^{-2} and to 24.18 mA cm^{-2}. The V_{OC} and FF are found to be at similar level of ca. 1.10 V and 78%, respectively. This indicates a general photocurrent enhancement upon incorporation of UCNP at this low concentration range. It should be noted that at concentration of 1.0 wt%, devices exhibit the highest PCE of 21.18%, with a J_{SC} of 24.41 mA cm^{-2}, V_{OC} of 1.104 V and FF of 78.6 % (**Fig. 3b**, this PCE is one of the highest values in the $MAPbI_3$-system based perovskite solar cells[43]). While with the increase of UCNP concentration to 5.0 wt%, there is an obvious drop in V_{OC} and FF, which can be ascribed to the insulating nature of the UCNP, where the series resistance (R_s) of the cell enlarges in proportion with the increased amount of UCNPs (as shown in **Fig. S5**).

These results suggest that by adding UCNPs into the perovskite, although there is no contribution from the upconversion mechanism, an overall improvement in J_{SC} has been observed in the devices (below concentration of 1.0 wt%) which may be related to other mechanisms such as electrical or optical modulations. To compare the electrical transport feature between the control and the composite film, we employed the conductive atomic force microscopy (c-AFM) to map the electrically conductive landscapes in dark condition for both samples (**Fig. S6**). **Fig. 3c** shows the statistics of the surface current collected in the c-AFM mapping in area of 5.0 × 5.0 μm region. We further use Gaussian function to fit the distribution and observe the similar average value and

standard deviation of the surface current. These results revealed that both samples exhibit similar electrical transport at microscopic scale. To further confirm this equivalence in electrical transport, we also estimate the electron mobility of the devices using space charge limited-current (SCLC) method. Electron-only diode with a structure of FTO/TiO_2/Perovskite/PCBM/Ag is used to measure the dark current density-voltage (J-V) characteristics, assuming that the measured current is related to single-type of carriers (i.e., electrons here). In principle, the current density and voltage follow a linear correlation (i.e., an Ohmic behavior with $J \propto V$) in the low bias voltage region. With further increase of bias voltage beyond the trap-filling limit (V_{TFL}), traps in the materials start to be filled by the injected charge carrier, where the current density and voltage exhibits a nonlinear correlation (i.e., trap-filling behavior with $J \propto V^n$, where $n \neq 1$). At a higher bias voltage when all the traps in the materials have been filled by injected charge carriers, the current density-voltage starts to show a quadratic relationship (i.e., $J \propto V^n$, where $n = 2$), entering the space charge limited-current (SCLC) region[44]. The *J-V* behavior can be then modeled by the Mott-Gurney law[45-46] as shown in equation of:

$$\mu = \frac{8JL^3}{9\varepsilon_0\varepsilon_r V^2} \qquad (2)$$

where μ is carrier mobility of electron, L is the perovskite film thickness, ε_0, ε_r are vacuum and relative permittivity of $MAPbI_3$, respectively, J is the current density, and V is the applied bias voltage. **Fig. 3d** and **3e** show the dark *J-V* curves of the electron-only diodes based on pristine $MAPbI_3$ and composite of $MAPbI_3$ with 1 wt% UCNP. The pristine $MAPbI_3$ sample shows a mobility of 2.1×10^{-5} cm^2 V^{-1} s^{-1}, consistent with the typical value for this material. The composite sample displays a similar value of 1.9×10^{-5} cm^2 V^{-1} s^{-1}. Hence, both samples show similar electrical transport behavior in dark. In order to investigate their behavior under illumination, we use the TIPL (Time-integrated photoluminescence) and TRPL (Time-resolved photoluminescence) spectroscopy to quantify the photoluminescent attributes. **Fig. 3f** shows the steady state TIPL spectra. As expected, both samples display similar PL intensity in range of 5×10^5 counts to 6.5×10^5 counts under identical excitation of light with wavelength of 506 nm. Interestingly, there is a slightly higher PL intensity observed in the composite sample compared to the control. **Fig. 3g** shows the TRPL of pristine $MAPbI_3$ and $MAPbI_3$ with 1 wt% UCNP film. To extract the lifetime information from the result, we utilized the following bi-exponential function[47] to fit the TRPL

$$f(t) = A_1 \exp\left(\frac{-t}{\tau_1}\right) + A_2 \exp\left(\frac{-t}{\tau_2}\right) + B \qquad (3)$$

where τ_1, τ_2 is the slow and fast carrier decay lifetime component, A_1, A_2 are their corresponding decay amplitudes, and B is a constant. The average photocarrier decay lifetime (τ_{ave}) can be obtained by using the equation below[48]:

$$\tau_{ave} = \frac{\sum A_i \tau_i^2}{\sum A_i \tau_i} \qquad (4)$$

As a result, the composite sample displays an $\tau_{ave,composite}$ of 80.24 ns, which is slightly higher than that of 67.20 ns from the pristine $MAPbI_3$. This is consistent to the result in the TIPL measurement. Overall, the electrical transport results indicate no obvious changes upon UCNP doping, while in the optical-related photophysical process we discovered a slightly boosted PL in the composite sample. These results suggest that the optical field distribution can be modulated by the UCNP.

Since the UCNP has distinct optical properties (e.g., refractive index, 1.47 vs. 2.71 of the $MAPbI_3$ perovskite), the light intensity distribution as well as the instant photocarrier distribution within the perovskite can be controlled by the UCNP. In order to understand how this mechanism can affect the photovoltaic process, we utilized the optical field simulation methods (finite element analysis using COMSOL)[49-50] to illustrate the effect. For modeling simplification, we constructed a 3D model with 0.5 μm× 0.5 μm in X-Y plane and a thickness of 500 nm in Z-direction (with multi-layer of FTO/TiO_2/$MAPbI_3$/Spiro-OMeTAD/Au), for both reference and composite samples (**Figs. 4a** and **4d**, respectively). In the composite, four nanoparticles are embedded in the film. **Figs. 4b** and **4e** present the simulated optical field distribution in pristine perovskite and composite films, projected on X-Z plane, respectively (projections on X-Z plane are also included in **Fig. S7**). It can be seen that the optical field distribution throughout the film thickness direction (Z-direction) is obviously different upon including nanoparticles. The pristine sample displays a gradient of optical field, quickly descending from the front side to the back contact. While the composite sample shows locally strengthened optical field near/between the nanoparticles inside of the film, compromising the gradient of optical field and making the optical field more homogeneously distributed along the Z-direction. We also made other simulation models with randomly distributed nanoparticles and found similar trend of much smaller gradient of optical field, i.e., a more uniform distribution of optical field along the thickness direction (**Fig. S8**).

Such a homogenization of optical field (HOF) can be beneficial for more efficient (i) photocarrier drift and (ii) collection with smaller recombination loss. As can be seen in **Fig. 4c**, in the pristine sample, at the surface region near the front side due to a large value of optical field,

the light intensity in this region (small z) is much larger than that in deeper regions (large z). In such scenario, photocarrier generation mainly occurs at the front surface region and consequently the photocarrier concentration will have a gradient along z-direction. In a n-i-p configuration, the photogenerated holes need to drift along the positive z-direction towards anode at the back contact. Thus, a large number of holes generated at the front surface region need to drift up to 500 nm (thickness of the perovskite film) to reach the anode. This process can be significantly affected by the point defects or traps as well as scattering during the transport in the perovskite film, as soon as it has a such a long distance to drift which exceed its average drifting limit ($D_{h,ref}$ in **Fig. 4c**). Secondly, the localized high concentration of photocarrier near the surface region increase the probability of bimolecular recombination, which will be discussed in detail in the later section. In comparison, after addition of nanomaterials, the light intensity is dispersed throughout the film, and it can vary upon changing the NP size and distribution. As shown in **Fig. 4f**, the HOF can lead to homogenized generation of photocarriers along the thickness of the film so that both the photogenerated electrons and holes can be dispersed more uniformly along the thickness direction and the drift pathway for holes is smaller in average. This can circumvent the abovementioned transport issues due to long drift pathway in the pristine sample.

In order to quantitively analyze this HOF effect, we extract the optical field strength |E| distribution within the solar cell device in **Fig. 4g**, using a 650 nm incident light as the light source with an intensity of 1.60 W m^{-2} consistent to the power density equivalent to the intensity of solar spectrum at 650 nm. The light intensity distribution within the film can then be calculated from the optical field strength |E| distribution (detailed in **Supplementary Note 3**). The as-generated photocarrier concentration rate can be obtained by equation

$$N_c(z) = \frac{EQE \cdot \lambda}{hc} \cdot \frac{E(z)^2}{2\mu_0 c} \qquad (5)$$

where λ is the wavelength of incident light, c is the light speed, h is Planck's constant, $E(z)$ is the electric field of light along the Z-direction of device, μ_0 is the magnetic permeability of free space, and EQE is the external quantum efficiency of the device at the wavelength of λ corresponding to that light intensity. In the example of **Fig. 4g**, the wavelength is 650 nm. In order to get the EQE profile with respect to the light intensity at constant wavelength of 650 nm, we measure the photocurrent density-light intensity (J-I) curve of the composite device in **Fig. 4h**. The light source is a 650 nm laser with optical filters of various optical densities. There is a linear dependence of photocurrent proportional to the light intensity. Hence, we regard the EQE value in **Equation 5** as

a constant (the value is extracted from EQE spectrum in **Fig. 2c**) for calculating the $N_c(z)$ profile. As a result, **Fig. 4i** compares the carrier density profile along the thickness direction for both samples. At the surface (z = 0), both display identical carrier density of 4×10^{17} cm^{-2} s^{-1} (we use area density here as we project it along Z-direction for profile analysis, and the unit [s^{-1}] is related to the time-dimension that can be regarded as 'rate' for understanding). As the z goes deeper into the film, the reference sample shows a linear decay with a large slope of 8×10^{21} cm^{-2} s^{-1}. In contrast, the composite film displays an interesting distribution with several peaks located deeper in the perovskite film. This indicates that in the film there are several sites with high photogeneration rate and consequently high concentration of as-generated photocarriers, which have a shorter pathway to electrode and consequently reduced loss during transport. We integrated the curve in **Fig. 4i**, which represents the overall photocarrier generation within the film. The composite film displays a higher density of generated photocarriers (15.3% higher than that of the pristine sample under 650 nm incident from this model), which can be ascribed to the light trapping effect with the presence of nanoparticles. Overall, using this simplified model, we find that this nanocrystal-perovskite composite can generate a HOF effect to minimize the carrier loss during drifting to electrodes and contribute to a higher photocurrent.

In order to cross-check the effectiveness of HOF in contributing to photocurrent, we then utilize similar nanoparticles of $NaYbF_4$ but without Tm doping, i.e., non-upconversion (NUC) nanoparticles (NPs) (**Fig. 5a**). **Fig. 5b** shows the TEM images of the $NaYbF_4$ NUC-NPs, where the particle size is of ca. 40 nm (the size is smaller than that of UCNP which is due to the random synthetic condition for NPs). **Fig. 5c** displays the PL and absorption spectrum of $NaYbF_4$ NPs, where there is a similar absorption peak as that of the $NaYb_{0.99}Tm_{0.01}F_4$ UCNP due to the presence of $^2F_{5/2}$ orbital of Yb in these $NaYbF_4$ NUC-NPs. Without the Tm doping, these $NaYbF_4$ NUC-NPs did not display a UC PL in the visible region from 350 nm to 800 nm. Hence, by incorporating the $NaYbF_4$ NUC-NPs into the perovskite, there should be no UC effect induced photocurrent gain, while the HOF can be present due to the similar refractive index and extinction coefficient between $NaYbF_4$ and $NaYb_{0.99}Tm_{0.01}F_4$. We then use these $NaYbF_4$ NUC-NPs as a variant to study their HOF contribution to photocurrent. **Fig. 5d** shows the cross-sectional SEM image of a n-i-p solar cell, where the NUC-NPs are well dispersed in the perovskite film. We test the solar cell performance under standard characterization procedure. **Fig. 5e** displays the photocurrent density-voltage (J-V) curve of the device using $MAPbI_3$ perovskite doped with 0.2 wt% $NaYbF_4$ NUC-

NPs under 1 sun illumination. The device displays a J_{SC} of 24.46 mA cm^{-2}, V_{OC} of 1.507 V, FF of 77.4% and PCE of 20.01%. This J_{SC} value is 1.53 mA cm^{-2} (ca. 7%) higher than that of 22.93 mA cm^{-2} from control device (**Fig. 2b**), and even higher than the device using same doping level of UCNPs (23.76 mA cm^{-2}). This could be due to the smaller size of the NPs which offers an enhanced HOF effect. To verify the accuracy of the J_{SC} value obtained from J-V curve, we measured the EQE spectrum (**Fig. 5f**) with an integrated photocurrent value of 24.05 mA cm^{-2}, which confirms the overall higher J_{SC} in the device using $NaYbF_4$ NUC-NPs.

In order to further confirm this trend, we conducted the statistical investigations on the J_{SC} by making multiple devices based on pristine $MAPbI_3$, $MAPbI_3$ with 0.2 wt% $NaYb_{0.99}Tm_{0.01}F_4$ UCNPs, and $MAPbI_3$ with 0.2 wt% $NaYbF_4$ NUC-NPs. There are total of 60 devices fabricated for all the groups and **Fig. 5g** shows the statistics for V_{OC}, FF, J_{SC} and PCEs. **Table S2** summarizes the photovoltaic parameters. As a result, compared to the pristine and UCNP doped perovskite device, the solar cells incorporating NUC-NPs display comparable V_{OC} and FF of 1.069 ± 0.013 V and 75.5 ± 1.5 %, respectively, but obviously higher J_{SC} of 24.13 ± 0.21 mA cm^{-2}. Even compared to the UCNP device, the NUC-NP device shows a 3% improved average J_{SC}. Since the NUC-NPs do not contribute to UC, there is no UC-generated photocurrent in the device. Instead, the $NaYbF_4$ NUC-NPs have refractive index and extinction coefficient of 1.47 and 2.4×10^{-5}, respectively, that are much different from those of $MAPbI_3$. This ensures the HOF effect in the composite film. Hence, the HOF induces more efficient photocarrier transport with less carrier losses leading to a higher J_{SC} in the $NaYbF_4$ NUC-NPs doped solar cells. Interestingly, we also observed that the NUC-NP device exhibits higher J_{SC} than the UCNP device. This is most likely due to the smaller size of the NUC-NP (ca. 40 nm) than the UCNP (ca. 140 nm). Since the weight ratio of 0.2 wt% is identical for both cases, there is a higher number of NPs in the composite compared to that of UCNPs in its corresponding composite. The well-dispersion of NUC-NPs in the film will provide a stronger HOF effect whereby a higher J_{SC}. We utilize the NUC-NPs and observe that the resultant devices also exhibit enhanced photocurrent, which can be ascribed to the HOF effect rather than the UC effect.

It should be noted that such HOF effect is a general photonic effect in high distinction coefficient solar cells such as perovskite. To further verify the universality of HOF, we also employ the commercial SiO_2 nanoparticles (S-NP) (**Fig. 6a**) to replace UCNP or NUC-NP followed by a bimolecular recombination investigation. Similar to those $NaYbF_4$-nased UCNPs, these SiO_2 NPs

also have smaller refractive index (n =1.47) than $MAPbI_3$ (n = 2.71), which lays down the foundation for triggering the HOF. In the meantime, we speculate that there are two direct sub-effects of HOF, i.e., (i) efficient photocarrier drift (has been discussed in **Fig. 4**) and (ii) reduced bimolecular recombination. Notably, in high-performance perovskite solar cells, the charge diffusion length in these perovskite thin films can reach to micrometer scale, indicating the less likely influenced by the '(i) efficient photocarrier drift' effect. Nevertheless, the bimolecular recombination can be the hypothetical loss pathways for photocarriers. Especially at the surface region where intensified light leads to much higher photocarrier concentration localized in this region. This could lead to strong bimolecular losses due to is square law to carrier concentration. In order to study if the '(ii) reduced bimolecular recombination' can significantly affect the device performance, we utilize a chloride-doped perovskite, i.e., $MAPbI_{3-x}Cl_x$ (x =0.05) that is of long carrier diffusion length (to minimize the drift concerns) for the solar cell fabrication. In brief, we obtained a higher baseline efficiency of 20.13% using this chloride-doped perovskite (**Fig. 6d**). And on this basis, we use two types of S-NPs to incorporate them in the perovskite. In the first approach, S-NPs was pre-dispersed in liquid phase of ethanol (denoted as S-NP(L)) and then added into perovskite precursor solution for subsequent spin-coating. In the second approach, S-NPs were in the dried powder form (denoted as S-NP(P)), which was directly mixed with perovskite precursor powders and made into solution for spin-coating. **Fig. 6b** and **Fig. 6c** show the cross-sectional SEM images of the solar cell device based on composite film of $MAPbI_{3-x}Cl_x$ (x =0.05) integrated with 0.1 wt. % of S-NP (L) and S-NP (P), respectively. The presence of S-NP (marked by blue color) embedding in the perovskite matrix is well observed. It is found that the S-NP(L) shows a more homogeneous distribution in the composite film while the S-NP(P) shows certain degree of aggregation inside the film. This can be due to the pre-dispersion step of S-NP(L) in ethanol that facilitates the homogeneous dispersion of nanoparticles in the precursor ink and reduces the degree of aggregation. **Fig. 6d** shows the J-V curves of these S-NP integrated device as well as the corresponding photovoltaic parameters (inset table), and **Fig. 6e**, **Fig. 6f**, **Fig. S9a** and **Fig. S9b** show the statistics of J_{SC}, PCE, V_{OC} and FF based on analysis of 20 devices, respectively. As a result, the pristine $MAPbI_{3-x}Cl_x$ (x=0.05) device displays a J_{SC} of 23.82 ± 0.16 mA cm^{-2}, V_{OC} of 1.106 ± 0.011 V, FF of 76.7 ± 0.6 % and a PCE of 20.20 ± 0.24 %. In comparison, the device doped with 0.1 wt.% of S-NP(L) displays a similar V_{OC} of 1.113 ± 0.008 V, FF of 76.7 ± 0.8 % but a significantly higher J_{SC} of 25.56 ± 0.23 mA cm^{-2}, which eventually lead to an

enhanced PCE of 21.82 ± 0.28 %. Compared with the S-NP(L), the device doped with S-NP(P) shows smaller enhancement of J_{SC} of 24.93 ± 0.21 mA cm^{-2} (vs. 25.56 ± 0.23 mA cm^{-2} for the device doped with S-NP(L)). This could be due to the nanoparticle aggregation that impairs the homogeneity of optical field distribution. We also check if the HOF effect is still valid on the high-performance device using the $NaYbF_4$ NUC-NP of larger size of ca. 115 nm (**Fig. S10a**). As shown in **Fig. S10b and S10c**, compared with pristine device, the device doped with 1 wt.% NUC-NP shows an improved J_{SC} of 24.37 ± 0.24 mA cm^{-2} larger than that of control. Overall, using the high mobility chloride-doped perovskite, we also observed this J_{SC} enhancement, which is applied for different types of NPs. These results revealed that such HOF effect can be a more general strategy to enhance the J_{SC} by introducing nanomaterials of distinct reflective index.

So far, the we found even using the long diffusion length perovskite ($MAPbI_{3-x}Cl_x$), the devices also exhibit a general J_{SC} enhancement upon various NPs. This can be understood by the secondary sub-effect of HOF, i.e., the '(ii) reduced bimolecular recombination'. In specific, in prior section, we have revealed that the HOF effect can decrease the drift pathway of photogenerated charges thus reduces the chance of scattering or recombination by defects and other charge traps (**Fig. 4**). This implies HOF effect is particularly useful for perovskite film of inferior quality which has high population of defects that is harmful for charge transport. However, in high-quality perovskite film with less defects, the free carrier diffusion length can be up to ~1 μm which exceeds the normal device thickness. This makes the HOF's sub-effect of '(i) efficient photocarrier drift' less effective because even the carrier generated deeply inside the film can be extracted easily due to the good transport property. However, it should also be noted that the photocarrier loss can still exist by following both the non-radiative recombination (also referred as trap-assisted recombination) and radiative recombination (also referred as biomolecular recombination) pathways. It has been admitted that halide perovskite film typically has high concentration of trap density (10^{14}–10^{17} cm^{-3}) that can lead to significant non-radiative recombination. However, the radiative recombination can also be significant as well because it is proportional to the product of photo-electron and hole. The rate from classic model is expressed by:

$$R_{rad} = k_{rad}(np - n_i^2) \qquad (6)$$

where R_{rad} refers to the radiative recombination rate, k_{rad} is the rate constant, n and p represents the concentration of photogenerated electrons and holes, respectively, and n_i refers to the

concentration of intrinsic carriers. Although the magnitude of k_{rad} is relatively small (in the order of 10^{-10} cm^{-3} s^{-1}), the square of photocarrier concentration can be large (n in the order of 10^{15} cm^{-3} for the device during working condition). Particularly at the surface region, high portion of the light is absorbed by a thin layer close to the surface, and this will make the radiative recombination loss non-negligible. In fact, the radiative recombination is considered to be the dominate recombination mechanism in direct bandgap semiconductors. The HOF effect provides the possibility to address losses from radiative recombination in perovskite photovoltaics as it can efficiently homogenize the local photocarrier concentration thus reduce the chance of radiative recombination. As illustrated in **Fig. S11a** and **Fig. S11c**, photocarrier will be heavily localized near the light incident area of pristine $MAPbI_3$ device due to the much intensive optical field near the surface region (**Fig. 4b**), which tends to induce heavy photocarrier loss as the radiative recombination rate is very high. In an ideal case, photocarrier should be evenly distributed along the depth of the photoactive layer to reduce the local carrier concentrating so that the radiative recombination rate can be minimized. In the NP-doped device photocarrier distribution in the photoactive layer will be more uniform (as illustrated in **Fig. S11b and S11d**) due to the homogenization of optical filed throughout the film (**Fig. 4f**). This effectively reduces the local photocarrier concentration thus reduce the chance of radiative recombination and eventually improves the device output. As a result of the suppressed radiative recombination loss, we have been able to further improve the PCE from 20.13 % to 22.09 %.

To experimentally verify this, we carry out an in-situ radiative detection measurement. **Fig. S12** shows the measurement setup, where the pristine $MAPbI_{3-x}Cl_x$ and S-NP(L) doped solar cell device is connected to a resistor as an external load to maintain an operation condition. The 505 nm excitation light was focused on the back side of device to excite the photocarriers. We controlled the excitation light intensity to a low dose to simulate the condition under solar radiation so that all the incident light can be used for photocarrier generation. A photo detector is used to collected the emitted light (filtered by a long pass filter) from the device. In principle, there are a few manifestations of photocarrier destiny. As illustrated in **Fig. 6g**, after being excited from valence band (VB) to conduction band (CB) [process (i)] and subsequent hot carrier cooling [process (ii)], there are mainly three pathways for photocarriers: extraction by charge extraction layer [process (iii)], trap-assisted (non-radiative) recombination [process (v)], and radiative recombination [process (iv)]. Direct observation of fluoresce can be an indication of losses of

photogenerated carriers along [process (iv)]. **Fig. 6h** shows the steady-state fluoresce spectra collected from the pristine and S-NP(L) doped device. Compared with the pristine device, a noticeable 6-fold decrease in the fluoresce intensity was observed in the S-NP(L) doped device, which suggests the number of photons from [process (iv)] is significantly reduced in the doped device. **Fig. 6i** shows the transient fluoresce spectra of the device upon a pulse excitation at 505 nm. The S-NP(L) doped device shows a nearly two-fold longer lifetime of 53.67 ns compared to that in pristine device (27.98 ns). The larger the lifetime reveals the larger lifetime of photoexcited electrons at the bottom of conduction band. This can be understood by the HOF effect that induced a more uniform distribution of photocarriers. Unlike the localized high carrier concentration in the pristine device (**Fig. S11c**), recombination losses are compromised in the doped device. These results have shown that the photocarrier losses by radiative recombination in the perovskite solar cell may not be neglected. The HOF can help to suppress such losses and provide an avenue to further enhance the performance.

Conclusion

At the beginning, we utilize the $NaYb_{0.99}Tm_{0.01}F_4$ UCNP (a classic UC nanomaterial) and $NaYbF_4$ NUC-NP as tools to quantitively discuss how much the UC contribution can boost the perovskite solar cell performance. We found due to the small absorption and quantum yield of UC, there is negligible contribution from UC effect to photocurrent. Instead, the generally observed photocurrent increasement can be ascribed to the effect of localized optical field rearrangement, i.e., the HOF effect. Such a HOF can lead to a more uniform distribution of photocarriers, which is significantly distinct to the sharp gradient distribution in pristine device. It should be noted that the HOF effect is related to the (i) difference in the optical properties of the host material and nanomaterials and (ii) the geometric layout of the composite (e.g., shape, size, density, and distribution of particles). The nanoparticle-embedded perovskite composite here is one of the examples to trigger the HOF. We have demonstrated the effectiveness of such HOF on solar cell performance improvement using a range of nanoparticles including UCNP, NUC-NP, and commercially SiO_2 NP. Optimization of the material and geometry will lead to enhanced HOF effect and photogeneration within the active layer. The homogenized distribution of photocarriers along the thickness direction can lead to less carrier losses from radiative recombination of local carriers or from trap-induced losses along with the transport. Consequently, this mechanism can

provide a relevant working principle for the widely observed higher photocurrent in solar cells using nanomaterials. Based on results reported here, we anticipate that a HOF mechanism provides promising route for improving applications such as nanoantenna, concentrated photovoltaics and photovoltaic converter for laser-based wireless energy transmission, where the optical field plays a very important role in device/system performance.

Associated Content

Supplementary Information

Materials and methods. Supplementary notes: Supplementary note 1 shows the energy level diagram of $NaYb_{0.99}Tm_{0.01}F_4$ UCNP and the corresponding emission band. Supplementary note 2 shows the detailed calculation of maximum current contributed by upconversion. Supplementary note 3 shows the detailed calculation of photocarrier population distribution within solar cell device.

Acknowledgement

The authors acknowledge the financial support from the Air Force Office of Scientific Research (AFOSR award number FA9550-20-1-0157). H. Wu and J. Y. acknowledge the support from the U.S. Department of Energy Award No. DE-SC0019844, under the STTR program (Prime – NanoSonic Inc.). D. Y. acknowledges the support from Norfolk State University through NSF-CREST grant number HRD 1547771. L. Z. acknowledges the support through NSF I/UCRC: Center for Energy Harvesting Materials and Systems (CEHMS) through award number IIP-1916707.

Disclaimer:

"This report was prepared as an account of work sponsored by an agency of the United States Government. Neither the United States Government nor any agency thereof, nor any of their employees, makes any warranty, express or implied, or assumes any legal liability or responsibility for the accuracy, completeness, or usefulness of any information, apparatus, product, or process disclosed, or represents that its use would not infringe privately owned rights. Reference herein to any specific commercial product, process, or service by trade name, trademark, manufacturer, or otherwise does not necessarily constitute or imply its endorsement, recommendation, or favoring

by the United States Government or any agency thereof. The views and opinions of authors expressed herein do not necessarily state or reflect those of the United States Government or any agency thereof."

Reference

1. Shockley, W.; Queisser, H. J., Detailed Balance Limit of Efficiency of P-N Junction Solar Cells. *Journal of Applied Physics* **1961,** *32* (3), 510.

2. Zhou, Z. G.; Chen, Q. S.; Bermel, P., Prospects for high-performance thermophotovoltaic conversion efficiencies exceeding the Shockley-Queisser limit. *Energ Convers Manage* **2015,** *97*, 63-69.

3. Semonin, O. E.; Luther, J. M.; Choi, S.; Chen, H.-Y.; Gao, J.; Nozik, A. J.; Beard, M. C., Peak external photocurrent quantum efficiency exceeding 100% via MEG in a quantum dot solar cell. *Science* **2011,** *334* (6062), 1530-1533.

4. Tayebjee, M. J.; McCamey, D. R.; Schmidt, T. W., Beyond Shockley–Queisser: molecular approaches to high-efficiency photovoltaics. *The journal of physical chemistry letters* **2015,** *6* (12), 2367-2378.

5. Rao, A.; Friend, R. H., Harnessing singlet exciton fission to break the Shockley–Queisser limit. *Nature reviews materials* **2017,** *2* (11), 1-12.

6. Ross Jr, R.; Smokler, M., Electricity from photovoltaic solar cells: Flat-Plate Solar Array Project final report. Volume VI: Engineering sciences and reliability. **1986**.

7. Albinsson, B.; Olesund, A., Untapping solar energy resources. *Nature Photonics* **2020,** *14* (9), 528-530.

8. De Wild, J.; Meijerink, A.; Rath, J.; Van Sark, W.; Schropp, R., Upconverter solar cells: materials and applications. *Energy & Environmental Science* **2011,** *4* (12), 4835-4848.

9. Würth, C.; Fischer, S.; Grauel, B.; Alivisatos, A. P.; Resch-Genger, U., Quantum yields, surface quenching, and passivation efficiency for ultrasmall core/shell upconverting nanoparticles. *Journal of the American Chemical Society* **2018,** *140* (14), 4922-4928.

10. Homann, C.; Krukewitt, L.; Frenzel, F.; Grauel, B.; Würth, C.; Resch-Genger, U.; Haase, M., $NaYF_4$: Yb, Er/$NaYF_4$ core/shell nanocrystals with high upconversion luminescence quantum yield. *Angewandte Chemie International Edition* **2018,** *57* (28), 8765-8769.

11. Niihori, Y.; Wada, Y.; Mitsui, M., Single Platinum Atom Doping to Silver Clusters Enables Near-Infrared-to-Blue Photon Upconversion. *Angewandte Chemie* **2021,** *133* (6), 2858-2863.

12. Mahboub, M.; Huang, Z.; Tang, M. L., Efficient infrared-to-visible upconversion with subsolar irradiance. *Nano letters* **2016,** *16* (11), 7169-7175.

13. Chen, X.; Peng, D.; Ju, Q.; Wang, F., Photon upconversion in core–shell nanoparticles. *Chemical Society Reviews* **2015,** *44* (6), 1318-1330.

14. Haase, M.; Schäfer, H., Upconverting nanoparticles. *Angewandte Chemie International Edition* **2011,** *50* (26), 5808-5829.

15. Kittel, C.; McEuen, P.; McEuen, P., *Introduction to solid state physics*. Wiley New York: 1996; Vol. 8.

16. Xie, Z.; Sun, S.; Yan, Y.; Zhang, L.; Hou, R.; Tian, F.; Qin, G., Refractive index and extinction coefficient of $NH_2CH=NH_2PbI_3$ perovskite photovoltaic material. *Journal of Physics: Condensed Matter* **2017,** *29* (24), 245702.

17. Yu, J.; Yang, Y.; Fan, R.; Liu, D.; Wei, L.; Chen, S.; Li, L.; Yang, B.; Cao, W., Enhanced Near-Infrared to Visible Upconversion Nanoparticles of Ho^{3+}-Yb^{3+}-F–Tri-Doped TiO_2 and Its Application in Dye-Sensitized Solar Cells with 37% Improvement in Power Conversion Efficiency. *Inorganic Chemistry* **2014,** *53* (15), 8045-8053.

18. Yuan, C.; Chen, G.; Li, L.; Damasco, J. A.; Ning, Z.; Xing, H.; Zhang, T.; Sun, L.; Zeng, H.; Cartwright, A. N., Simultaneous multiple wavelength upconversion in a core–shell nanoparticle for enhanced near infrared light harvesting in a dye-sensitized solar cell. *ACS applied materials & interfaces* **2014,** *6* (20), 18018-18025.

19. Ma, X.; Ni, X., Using upconversion nanoparticles to improve photovoltaic properties of poly (3-hexylthiophene)–TiO_2 heterojunction solar cell. *Journal of nanoparticle research* **2013,** *15* (4), 1-7.

20. Kesavan, A. V.; Kumar, M.; Rao, A. D.; Ramamurthy, P. C., Light management through up-conversion and scattering mechanism of rare earth nanoparticle in polymer photovoltaics. *Optical Materials* **2019,** *94*, 286-293.

21. He, M.; Pang, X.; Liu, X.; Jiang, B.; He, Y.; Snaith, H.; Lin, Z., Monodisperse dual-functional upconversion nanoparticles enabled near-infrared organolead halide perovskite solar cells. *Angewandte Chemie* **2016,** *128* (13), 4352-4356.

22. Park, J.; Kim, K.; Jo, E. J.; Kim, W.; Kim, H.; Lee, R.; Lee, J. Y.; Jo, J. Y.; Kim, M. G.; Jung, G. Y., Plasmon enhanced up-conversion nanoparticles in perovskite solar cells for effective utilization of near infrared light. *Nanoscale* **2019,** *11* (47), 22813-22819.

23. Gibart, P.; Auzel, F.; Guillaume, J. C.; Zahraman, K., Below band-gap IR response of substrate-free GaAs solar cells using two-photon up-conversion. *Japanese journal of applied physics* **1996,** *35* (8R), 4401.

24. Richards, B. S.; Shalav, A., Enhancing the near-infrared spectral response of silicon optoelectronic devices via up-conversion. *IEEE Transactions on Electron Devices* **2007,** *54* (10), 2679-2684.

25. de Wild, J.; Rath, J.; Meijerink, A.; Van Sark, W.; Schropp, R., Enhanced near-infrared response of a-Si: H solar cells with β-$NaYF_4$: Yb^{3+} (18%), Er^{3+} (2%) upconversion phosphors. *Solar energy materials and solar cells* **2010,** *94* (12), 2395-2398.

26. Shan, G. B.; Demopoulos, G. P., Near-infrared sunlight harvesting in dye-sensitized solar cells via the insertion of an upconverter-TiO_2 nanocomposite layer. *Advanced materials* **2010,** *22* (39), 4373-4377.

27. Ma, X.; Ni, X., Fabrication of polythiophene–TiO_2 heterojunction solar cells coupled with upconversion nanoparticles. *Journal of Materials Science: Materials in Electronics* **2015,** *26* (2), 1129-1135.

28. Schoenauer Sebag, M.; Hu, Z.; de Oliveira Lima, K.; Xiang, H.; Gredin, P.; Mortier, M.; Billot, L.; Aigouy, L.; Chen, Z., Microscopic evidence of upconversion-induced near-infrared light harvest in hybrid perovskite solar cells. *ACS Applied Energy Materials* **2018,** *1* (8), 3537-3543.

29. Cao, Y.; Zheng, X.; De Camillis, S.; Shi, B.; Piper, J. A.; Packer, N. H.; Lu, Y., Light-emitting diode excitation for upconversion microscopy: a quantitative assessment. *Nano Letters* **2020,** *20* (12), 8487-8492.

30. Chen, X.; Jin, L.; Kong, W.; Sun, T.; Zhang, W.; Liu, X.; Fan, J.; Yu, S. F.; Wang, F., Confining energy migration in upconversion nanoparticles towards deep ultraviolet lasing. *Nature communications* **2016,** *7* (1), 1-6.

31. Liu, Q.; Zhang, Y.; Peng, C. S.; Yang, T.; Joubert, L. M.; Chu, S., Single upconversion nanoparticle imaging at sub-10 W cm^{-2} irradiance. *Nature photonics* **2018,** *12* (9), 548-553.

32. Wu, C.; Wang, K.; Li, J.; Liang, Z.; Li, J.; Li, W.; Zhao, L.; Chi, B.; Wang, S., Volatile solution: the way toward scalable fabrication of perovskite solar cells? *Matter* **2021,** *4* (3), 775-793.

33. Wang, K.; Wu, C.; Hou, Y.; Yang, D.; Li, W.; Deng, G.; Jiang, Y.; Priya, S., A Nonionic and Low-Entropic MA $(MMA)_nPbI_3$-Ink for Fast Crystallization of Perovskite Thin Films. *Joule* **2020**.

34. Wang, K.; Wu, C.; Hou, Y.; Yang, D.; Ye, T.; Yoon, J.; Sanghadasa, M.; Priya, S., Isothermally crystallized perovskites at room-temperature. *Energy & Environmental Science* **2020**.

35. Oku, T., Crystal structures of $CH_3NH_3PbI_3$ and related perovskite compounds used for solar cells. *Solar Cells-New Approaches and Reviews* **2015,** *1*.

36. Hou, Y.; Wu, C.; Yang, D.; Wang, K.; Ye, T.; Brownlie, L.; Wang, K.; Priya, S., *Artemisinin* (ART)-Induced "perovskite/perovskite" bilayer structured photovoltaics. *Nano Energy* **2020,** *78*, 105133.

37. Wu, C.; Li, H.; Yan, Y.; Chi, B.; Felice, K. M.; Moore, R. B.; Magill, B. A.; Mudiyanselage, R. R.; Khodaparast, G. A.; Sanghadasa, M., Highly-Stable Organo-Lead Halide Perovskites Synthesized Through Green Self-Assembly Process. *Solar RRL* **2018,** *2* (6), 1800052.

38. Wu, C.; Wang, K.; Yan, Y.; Yang, D.; Jiang, Y.; Chi, B.; Liu, J.; Esker, A. R.; Rowe, J.; Morris, A. J., Fullerene Polymer Complex Inducing Dipole Electric Field for Stable Perovskite Solar Cells. *Advanced Functional Materials* **2019,** *29* (12), 1804419.

39. Hou, Y.; Wang, K.; Yang, D.; Jiang, Y.; Yennawar, N.; Wang, K.; Sanghadasa, M.; Wu, C.; Priya, S., Enhanced performance and stability in DNA-perovskite heterostructure-based solar cells. *ACS Energy Letters* **2019,** *4* (11), 2646-2655.

40. Nadort, A.; Sreenivasan, V. K.; Song, Z.; Grebenik, E. A.; Nechaev, A. V.; Semchishen, V. A.; Panchenko, V. Y.; Zvyagin, A. V., Quantitative imaging of single upconversion nanoparticles in biological tissue. *PloS one* **2013,** *8* (5), e63292.

41. Bharmoria, P.; Bildirir, H.; Moth-Poulsen, K., Triplet–triplet annihilation based near infrared to visible molecular photon upconversion. *Chemical Society Reviews* **2020,** *49* (18), 6529-6554.

42. Amemori, S.; Sasaki, Y.; Yanai, N.; Kimizuka, N., Near-infrared-to-visible photon upconversion sensitized by a metal complex with spin-forbidden yet strong S0–T1 absorption. *Journal of the American Chemical Society* **2016,** *138* (28), 8702-8705.

43. Yang, D.; Zhang, X.; Wang, K.; Wu, C.; Yang, R.; Hou, Y.; Jiang, Y.; Liu, S.; Priya, S., Stable Efficiency Exceeding 20.6% for Inverted Perovskite Solar Cells through Polymer-Optimized PCBM Electron-Transport Layers. *Nano letters* **2019**.

44. Murgatroyd, P., Theory of space-charge-limited current enhanced by Frenkel effect. *Journal of Physics D: Applied Physics* **1970,** *3* (2), 151.

45. Leighton, P. A., Electronic processes in ionic crystals (Mott, N F; Gurney, R W). ACS Publications: 1941.

46. Yang, D.; Yang, R.; Wang, K.; Wu, C.; Zhu, X.; Feng, J.; Ren, X.; Fang, G.; Priya, S.; Liu, S. F., High efficiency planar-type perovskite solar cells with negligible hysteresis using EDTA-complexed SnO_2. *Nature communications* **2018,** *9* (1), 3239.

47. Feng, J.; Zhu, X.; Yang, Z.; Zhang, X.; Niu, J.; Wang, Z.; Zuo, S.; Priya, S.; Liu, S.; Yang, D., Record efficiency stable flexible perovskite solar cell using effective additive assistant strategy. *Advanced Materials* **2018,** *30* (35), 1801418.

48. Jiang, J.; Wang, Q.; Jin, Z.; Zhang, X.; Lei, J.; Bin, H.; Zhang, Z. G.; Li, Y.; Liu, S., Polymer Doping for High-Efficiency Perovskite Solar Cells with Improved Moisture Stability. *Advanced Energy Materials* **2018,** *8* (3), 1701757.

49. Yang, D.; Zhang, X.; Hou, Y.; Wang, K.; Ye, T.; Yoon, J.; Wu, C.; Sanghadasa, M.; Liu, S. F.; Priya, S., 28.3%-efficiency perovskite/silicon tandem solar cell by optimal transparent electrode for high efficient semitransparent top cell. *Nano Energy* **2021,** *84*, 105934.

50. Raja, W.; Schmid, M.; Toma, A.; Wang, H.; Alabastri, A.; Proietti Zaccaria, R., Perovskite nanopillar array based tandem solar cell. *ACS Photonics* **2017,** *4* (8), 2025-2035.

Figures and captions

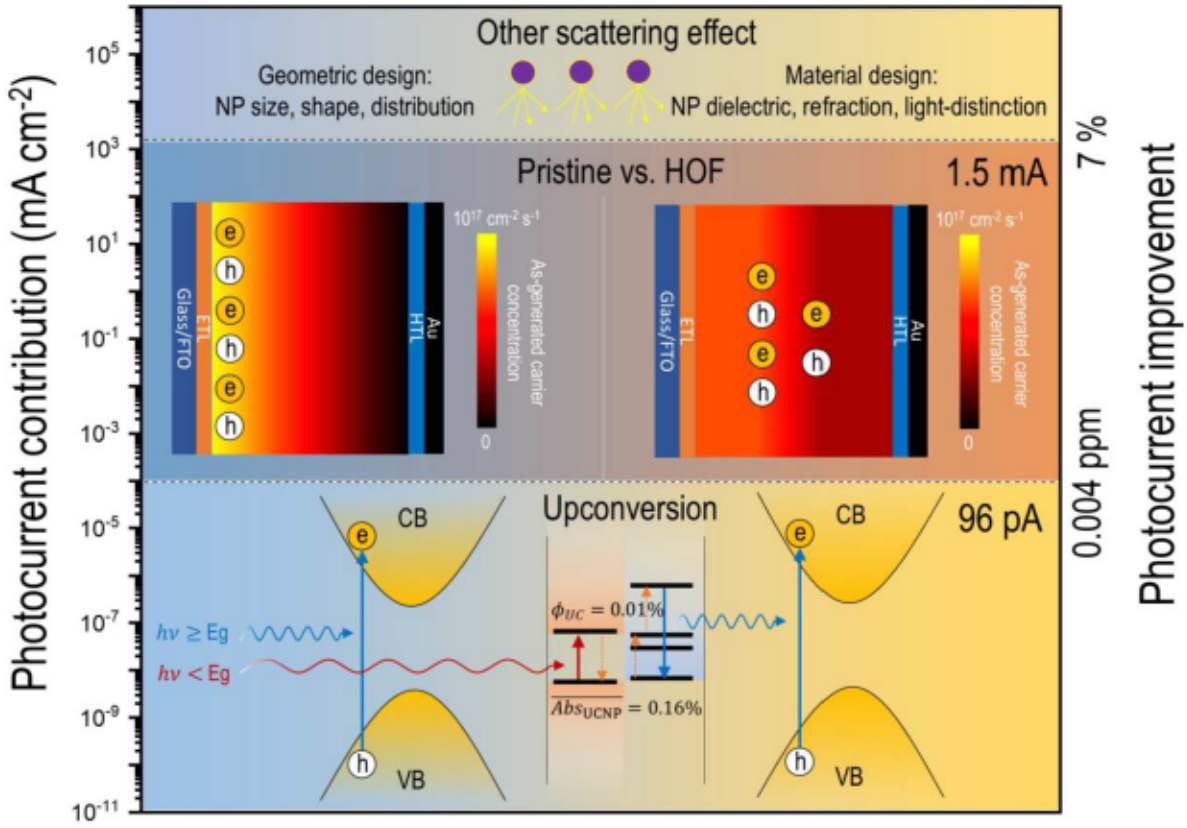

Scheme 1: Comparison between different mechanisms that drive the contribution to photocurrent: the upconversion mechanism recycle the in-band transparent light ($h\nu$< Eg), while due to the low upconversion efficiency of the state-of-the-art UCNP materials, the photocurrent contribution from this upconversion has a up limit of 96 pA on 1 cm^2 area. In contrast, HOF effect redistributes the optical field along the film thickness direction, which triggers a more uniform distribution of photocarrier generation site and thus more balanced photocarrier drift towards corresponding electrodes. This can reduce the carrier loss and lead to a 1.5 mA cm^{-2} enhancement in photocurrent, i.e., 7% contribution to photocurrent density. Beyond this, we anticipate additional scattering effects by proposed strategies such as NP shape-, size-, distribution-modification, and dielectric, refraction, light-distinction coefficient engineering, etc., there is a potential to trigger higher photocurrent exceeding the SQ limit.

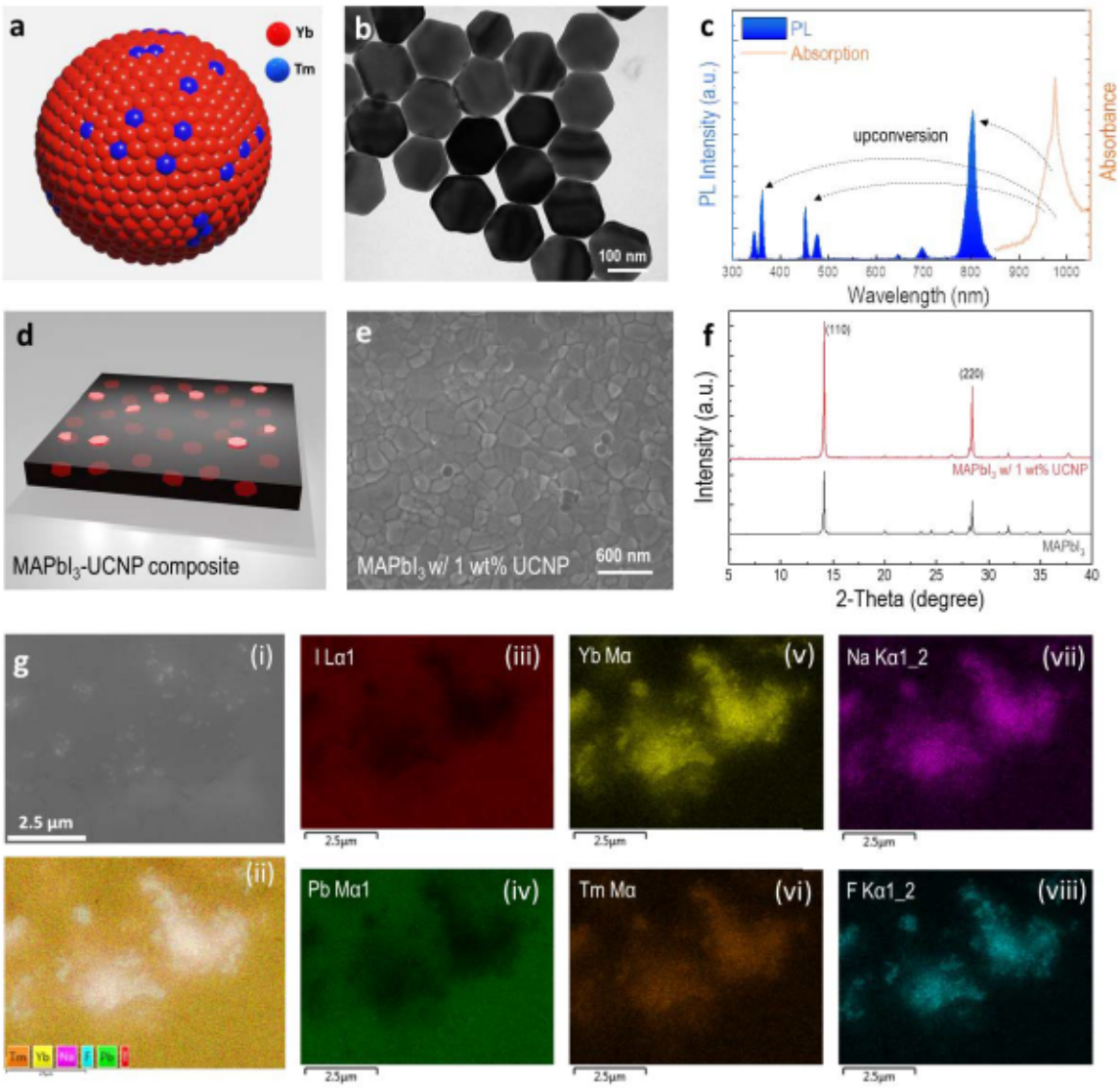

Figure 1: **$MAPbI_3$-UCNP composites** (a) Schematic description of $NaYb_{0.99}Tm_{0.01}F_4$ upconversion nanoparticles (UCNPs). For simplicity, the Na and F atoms are not shown. (b) TEM images of UCNPs (c) Upconversion (UC) Photoluminescence (PL) with 980 nm laser excitation and absorption spectrum of UCNPs film, excited at 980 nm (d) Schematic description for $MAPbI_3$-UCNP composite where UCNPs are embedded in the perovskite film matrix. (e) SEM image of $MAPbI_3$-UCNP film. (f) XRD spectra of pristine and UCNP-integrated $MAPbI_3$ film. (g) Energy-dispersive X-ray spectroscopy (EDS) mapping of $MAPbI_3$-UCNP composite film showing the UCNPs embedded within $MAPbI_3$ matrix.

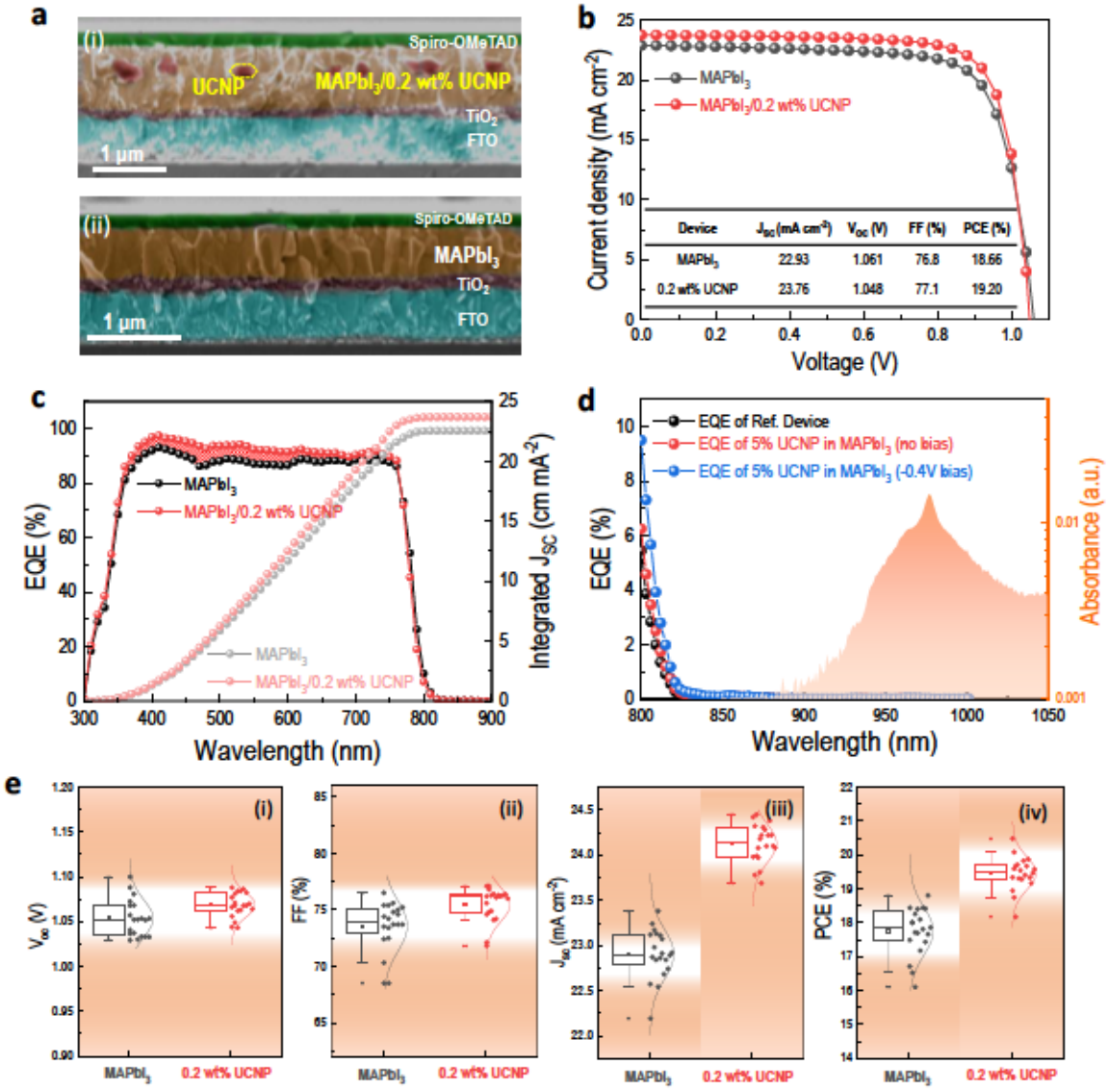

Figure 2: $MAPbI_3$-UCNP solar cell (a) Cross-sectional SEM image of $MAPbI_3$-UCNP and pristine $MAPbI_3$ solar cells with an n-i-p structure (TiO_2/Perovkskite/Spiro-OMeTAD). (b) J-V curves of pristine $MAPbI_3$ and UCNP-integrated solar cells under standard 1 sun illumination. (c) External quantum efficiency (EQE) spectra of pristine and UCNP-integrated $MAPbI_3$ solar cells (d) Zoom-in view of IPCE spectrum within UCNP absorption region showing negligible contribution from upconversion. (e) Performance parameters of pristine and UCNP-integrated solar cells: (i) V_{OC} (ii) FF (iii) J_{SC} and (iv) PCE.

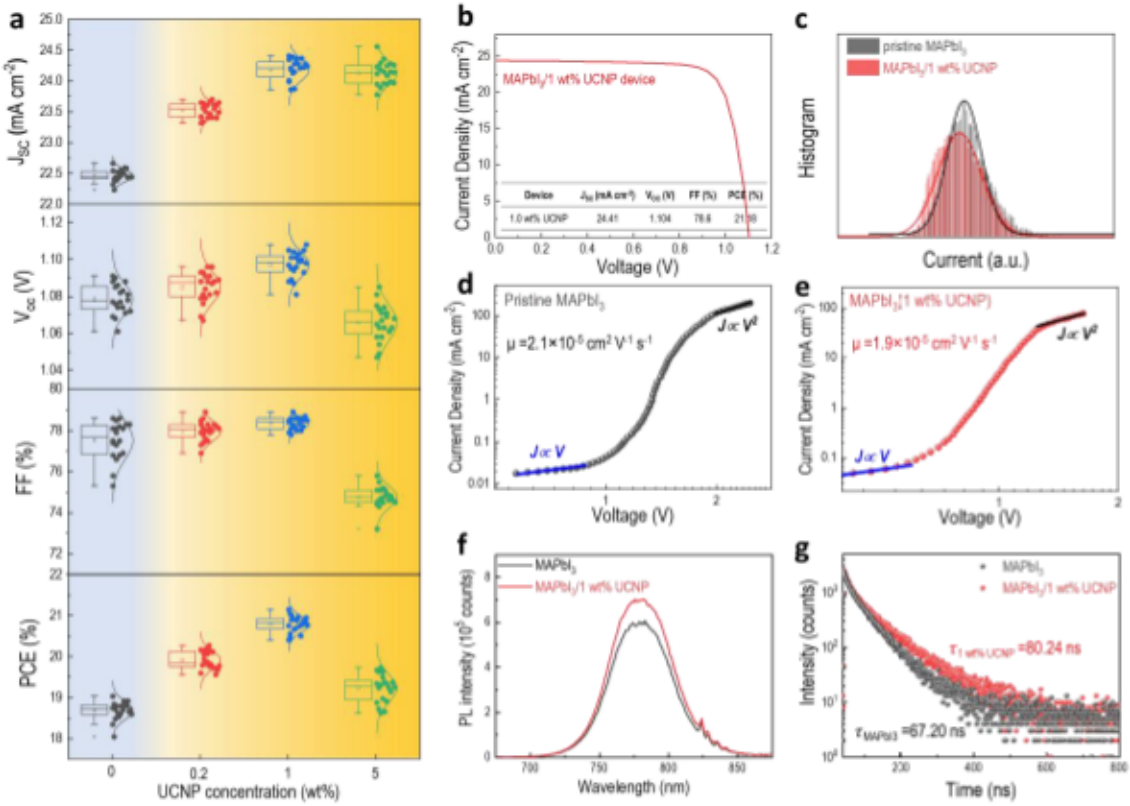

Figure 3: Contribution of UCNP on solar cell performance (a) Performance parameters of perovskite solar cells with different UCNP concentrations. (b) J-V curve of solar cells based on pristine and $MAPbI_3$ integrated with 1 wt% UCNP ($MAPbI_3$/1 wt% UCNP) under standard 1 sun illumination. (c) Current histogram profile of pristine $MAPbI_3$ and $MAPbI_3$/1 wt% UCNP film measured by conductive-AFM (d)-(e): J–V characteristic of the electron-only diode based on (d) pristine $MAPbI_3$ and (e) $MAPbI_3$/1 wt% UCNP film measured in the dark condition. (f)-(g): (f) Time-integrated PL spectra and (g) Time-resolved PL spectra of pristine $MAPbI_3$ and $MAPbI_3$/1 wt% UCNP film.

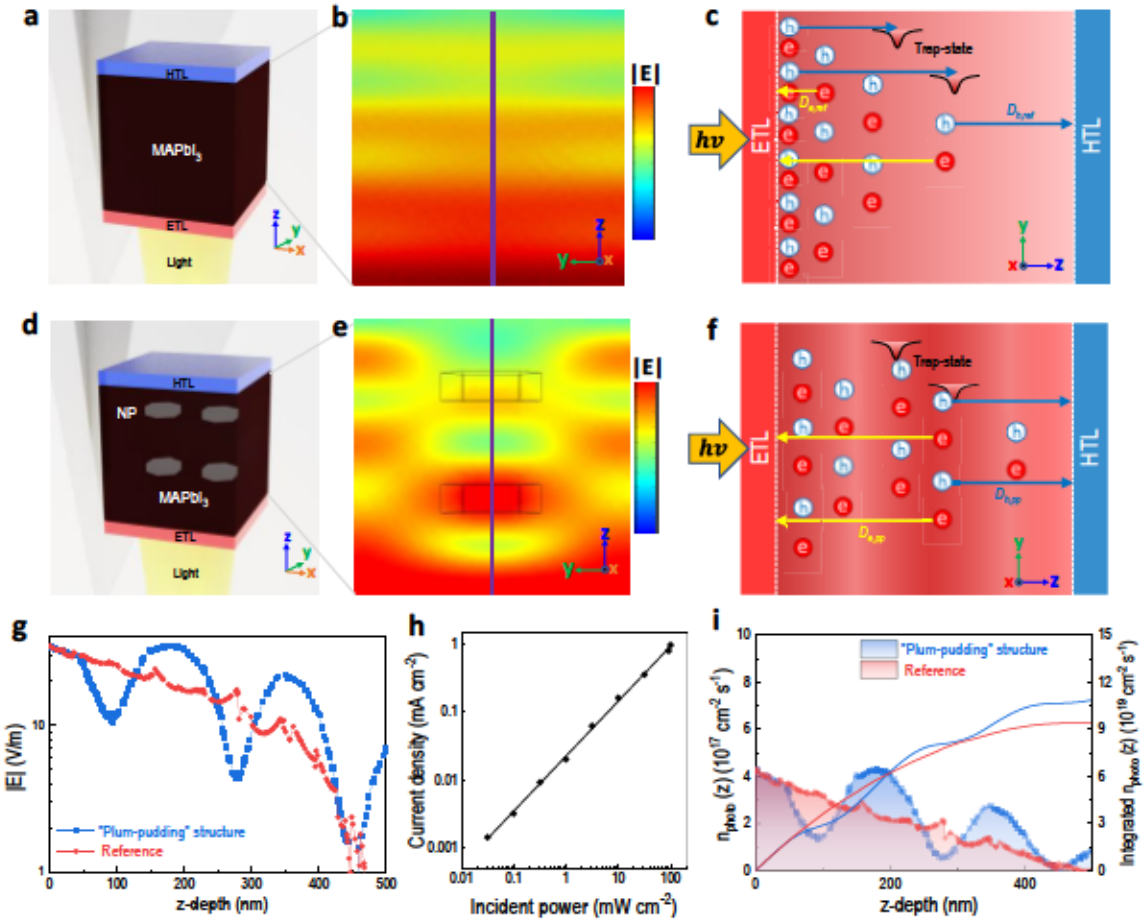

Figure 4: Optical field modulation (OFM) effect by UCNPs. (a) and (d): 3D model of (a) pristine $MAPbI_3$ film and (d) $MAPbI_3$-UCNP composite structure. (b) and (e): Simulation of optical field distribution of an incident 650 nm light within the (b) pristine $MAPbI_3$ device (e) $MAPbI_3$-UCNP device. The color indicates the magnitude of optical field strength |E|. (c) and (f): Schematic illustration of distribution of photocarriers due to the OFM effect and their subsequent drift towards ETL and HTL in (c) pristine $MAPbI_3$ device and (f) $MAPbI_3$-UCNP device. D_e and D_h refers to the drift distance for photo-generated electrons and holes, respectively. (g)-(i): (g) Simulation showing the distribution of optical field strength |E| within the solar cell device, assuming a 650 nm incident light from solar spectrum with an intensity of 1.60 W/m^2 (h) Current density with illumination power curve showing the linearity of solar cell device with respect to incident light power. (i) The estimated distribution of photocarrier density (n_{photon} (z)) as well as the integrated photocarrier density along the depth (z) of solar cell device.

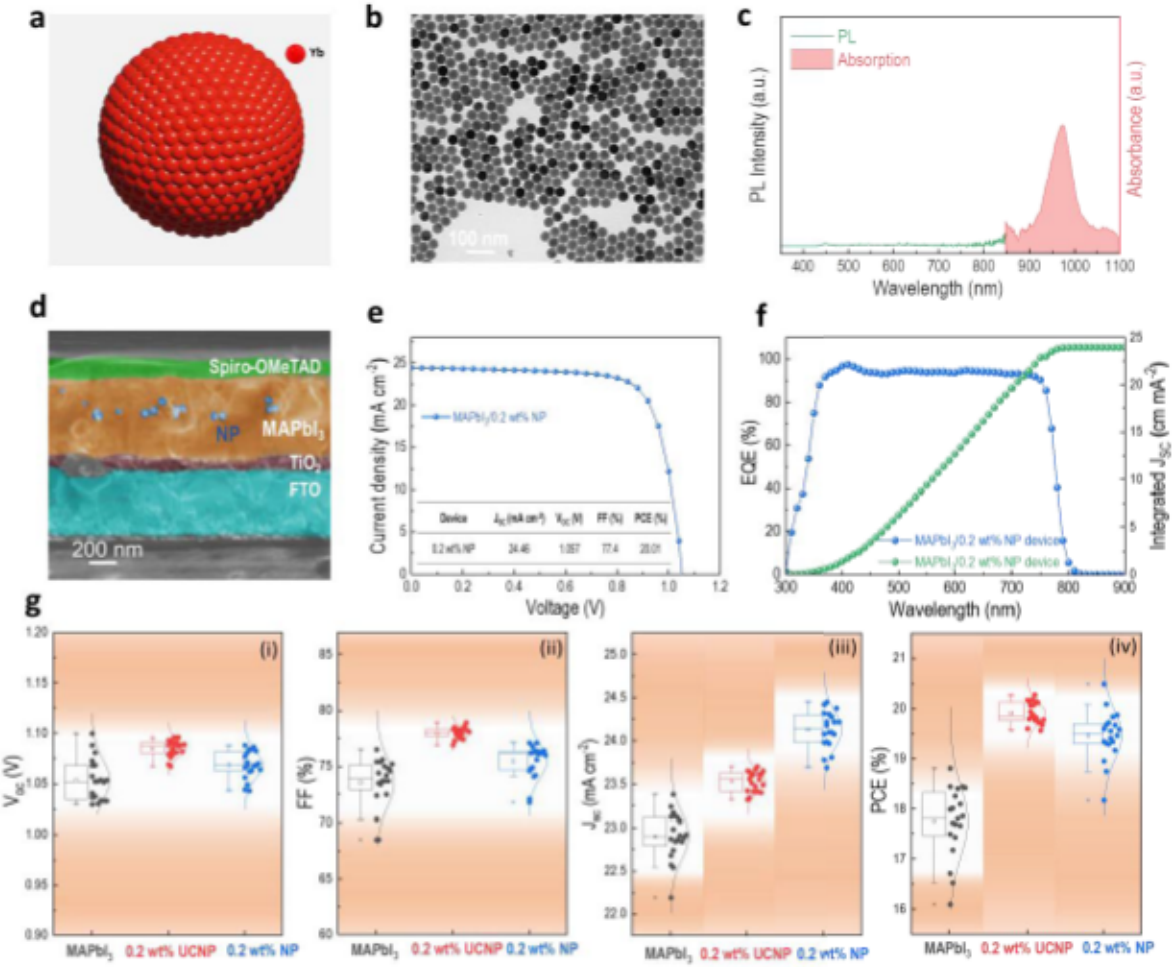

Figure 5: Solar cell performance of $MAPbI_3$ integrated with $NaYbF_4$ NUC NPs (a) Schematics for non-Tm doped $NaYbF_4$ non-upconversion nanoparticles (NUC NPs). For simplicity, the Na and F atoms are not shown. (b) TEM images of $NaYbF_4$ NUC NPs (c) UC Photoluminescence and absorption spectrum of $NaYbF_4$ NUC NPs, excited at 980 nm. (d) Cross-sectional SEM images of perovskite solar cell integrated with $NaYbF_4$ NUC NPs. (e) J-V curves of pristine $MAPbI_3$ and $NaYbF_4$ NP-integrated solar cells under standard 1 sun illumination. (f) External quantum efficiency (EQE) spectra of pristine and $NaYb_4$ NUC NP-integrated $MAPbI_3$ solar cells (g) Performance parameters of pristine and $NaYbF_4$ NUC NP-integrated solar cells: (i) V_{OC} (ii) FF (iii) J_{SC} and (iv) PCE.

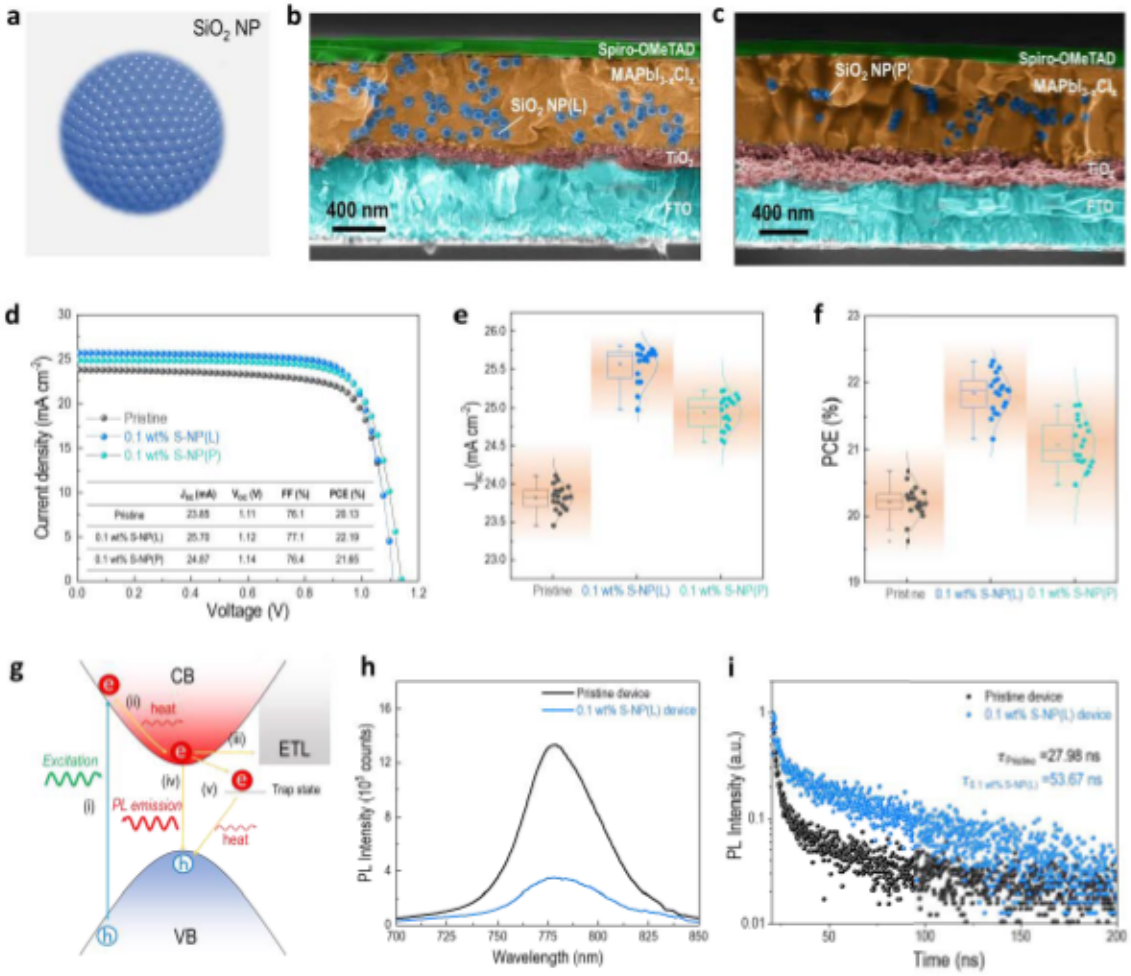

Figure 6: Solar cell performance of $MAPbI_{3-x}Cl_x$ (x=0.05) integrated with SiO_2 nanoparticle (S-NP): (a) Scheme of the commercial SiO_2 nanoparticle with a size of ~60 nm. (b)(c) Cross-sectional SEM images of SiO_2 nanoparticles (S-NP) embedded in $MAPbI_{3-x}Cl_x$ perovskite photoactive layer. Two types of S-NP were used: (b) S-NP pre-dispersed in ethanol (denoted as S-NP(L)) (c) S-NP dried powder (denoted as S-NP(P)). (d) J-V curves of pristine $MAPbI_{3-x}Cl_x$ device and device integrated by 0.1 wt% of S-NP(L) and 0.1 wt% S-NP(P). (e)(f) Statistics of the (e) J_{SC} and (f) PCE of pristine $MAPbI_{3-x}Cl_x$ device and device integrated by 0.1 wt% of S-NP(L) and 0.1 wt% S-NP(P). (g) Schematic illustration of the photovoltaic process and pathways for photoelectron: (i) light excitation (ii) hot carrier relaxation (iii) charge extraction by electron transport layer (iv) radiative recombination of photoelectron (v) trap-assisted recombination of photoelectron. (h)(i): (h) Steady-state PL emission spectra and (i) Time-resolved PL spectra collected from pristine $MAPbI_{3-x}Cl_x$ device and device integrated by 0.1 wt% S-NP(L) under operational condition.